AGU PUBLICATIONS

Geochemistry, Geophysics, Geosystems

RESEARCH ARTICLE
10.1002/2016GC006528

**Key Points:**
- Continuous monitoring of transient gas bubble emissions over 1 year was enabled by the NEPTUNE cabled observatory
- Flare onsets were triggered and controlled by tidally induced bottom pressure changes
- Decreasing pressure allowing gas to migrate and shifting the CH4 solubility in pore waters leads to ebullition

**Supporting Information:**
- Figure S1
- Table S1
- Movie S1

**Correspondence to:**
M. Römer,
mroemer@marum.de

**Citation:**
Römer, M., M. Riedel, M. Scherwath, M. Heesemann, and G. D. Spence (2016), Tidally controlled gas bubble emissions: A comprehensive study using long-term monitoring data from the NEPTUNE cabled observatory offshore Vancouver Island, *Geochem. Geophys. Geosyst.*, *17*, 3797–3814, doi:10.1002/2016GC006528.

Received 11 JUL 2016
Accepted 9 SEP 2016
Accepted article online 15 SEP 2016
Published online 29 SEP 2016



# Tidally controlled gas bubble emissions: A comprehensive study using long-term monitoring data from the NEPTUNE cabled observatory offshore Vancouver Island

**Miriam Römer[1], Michael Riedel[2], Martin Scherwath[3], Martin Heesemann[3], and George D. Spence[4]**

[1]MARUM-Center for Marine Environmental Sciences and Department of Geosciences, University of Bremen, Germany, [2]GEOMAR Helmholtz Centre for Ocean Research Kiel, Germany, [3]Ocean Networks Canada, University of Victoria, British Columbia, Canada, [4]School of Earth and Ocean Sciences, University of Victoria, British Columbia, Canada

**Abstract** Long-term monitoring over 1 year revealed high temporal variability of gas emissions at a cold seep in 1250 m water depth offshore Vancouver Island, British Columbia. Data from the North East Pacific Time series Underwater Networked Experiment observatory operated by Ocean Networks Canada were used. The site is equipped with a 260 kHz Imagenex sonar collecting hourly data, conductivity-temperature-depth sensors, bottom pressure recorders, current meter, and an ocean bottom seismograph. This enables correlation of the data and analyzing trigger mechanisms and regulating criteria of gas discharge activity. Three periods of gas emission activity were observed: (a) short activity phases of few hours lasting several months, (b) alternating activity and inactivity of up to several day-long phases each, and (c) a period of several weeks of permanent activity. These periods can neither be explained by oceanographic conditions nor initiated by earthquakes. However, we found a clear correlation of gas emission with bottom pressure changes controlled by tides. Gas bubbles start emanating during decreasing tidal pressure. Tidally induced pressure changes also influence the subbottom fluid system by shifting the methane solubility resulting in exsolution of gas during falling tides. These pressure changes affect the equilibrium of forces allowing free gas in sediments to emanate into the water column at decreased hydrostatic load. We propose a model for the fluid system at the seep, fueled by a constant subsurface methane flux and a frequent tidally controlled discharge of gas bubbles into the ocean, transferable to other gas emission sites in the world's oceans.

## 1. Introduction

Natural marine gas bubble emissions have been found at numerous sites around the world ocean margins, providing an effective transport pathway for light hydrocarbons from the sediments into the water column. Several studies focused on quantifying the amount of emanating gas entering the hydrosphere, e.g. in the Black Sea [*Nikolovska et al.*, 2008; *Greinert et al.*, 2010; *Römer et al.*, 2012a; *Sahling et al.*, 2009], the Makran continental margin [*Römer et al.*, 2012b], the Cascadia margin at southern Hydrate Ridge [*Torres et al.*, 2002], as well as the Håkon Mosby mud volcano [*Sauter et al.*, 2006]. The fraction of released methane reaching the sea-air boundary was studied in order to evaluate its contribution to climate warming as powerful greenhouse gas in the atmosphere [e.g., *Greinert et al.*, 2010; *Leifer and Patro*, 2002; *Leifer and Judd*, 2015; *McGinnis et al.*, 2006; *Shakova et al.*, 2010]. Most studies providing methane flow quantifications, however, do not account for spatial and temporal variability, due to the fact that short-term observations and measurements were usually acquired during research cruises limiting the time for experiments. But natural gas emissions have been most often observed to be highly transient in a variety of time scales [e.g., *Boles et al.*, 2001; *Kannberg et al.*, 2013; *Tryon et al.*, 1999; *Varadharajan and Hemond*, 2012]. Long-term monitoring, as such provided by Ocean Networks Canada's cabled ocean observatory [*Barnes et al.*, 2011], is therefore essential to appraise flux calculations and allow estimating uncertainties. Besides a better understanding of the magnitudes of gas bubble emissions variability, the factors influencing the observed changes in flux activation and triggering are still largely debated. Methane fluxes might be controlled by fluid flow rates mediated by microbial processes in marine sediments or physical changes in bottom pressure [*Fechner-Levy and Hemond*, 1996; *Leifer and Boles*, 2005; *Scandella et al.*, 2011], which can be influenced by e.g., bottom water currents, storms, tides, or swell. Furthermore, a correlation of fluid emissions with earthquakes has

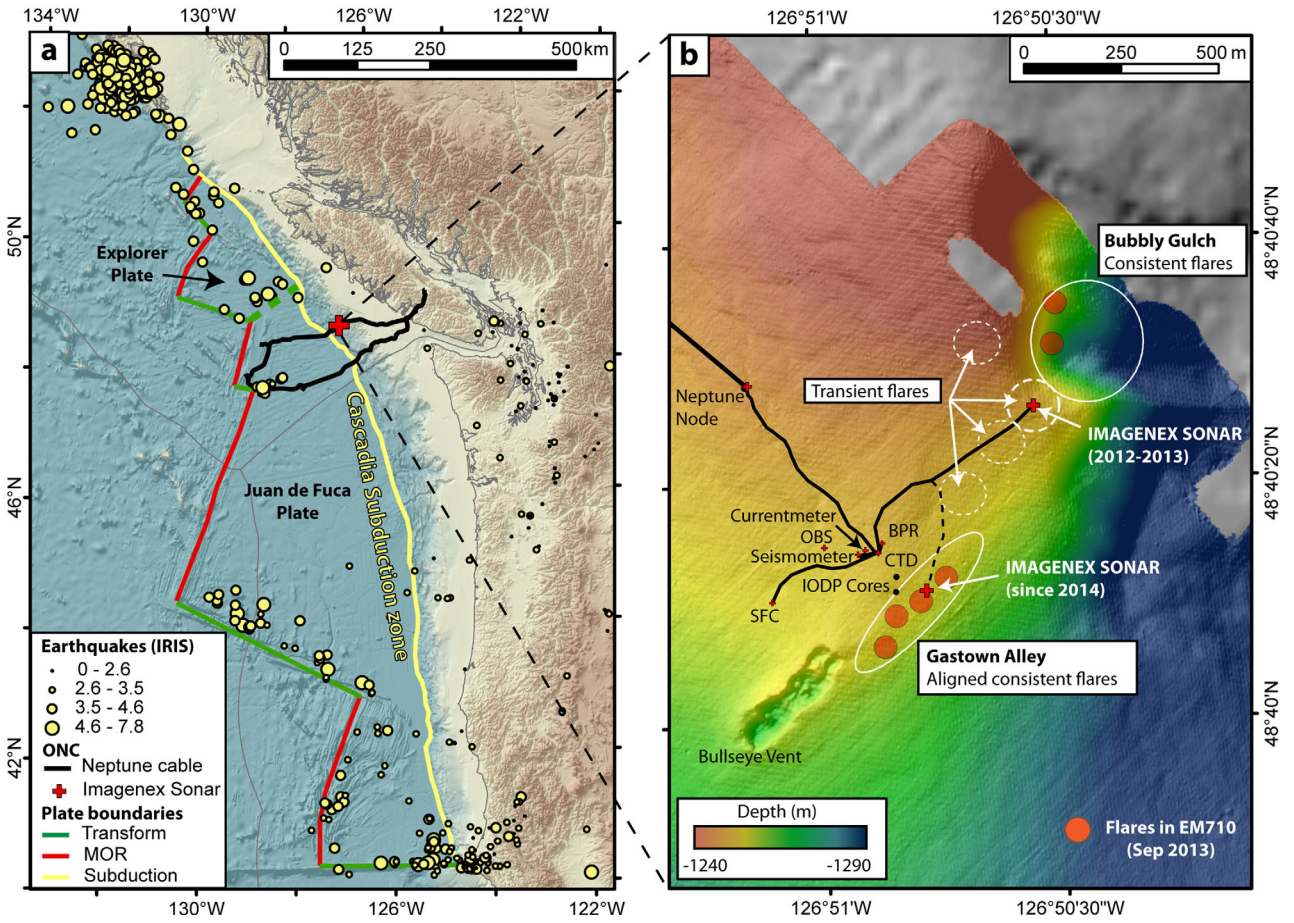


**Figure 1.** Overview of the study area. (a) Map of the Cascadia subduction zone including the plate boundaries and earthquake centers from June 2012 to July 2013. The backbone cable of Ocean Networks Canada's cabled observatory NEPTUNE is installed at the seafloor in a loop shape connecting the shore station on Vancouver Island over the entire continental margin with the mid-ocean ridge (MOR). (b) The IMAGENEX sonar is located in a seep area at the so-called Clayoquot Slope node site and connected to the NEPTUNE cable.

been postulated in several studies [*Fischer et al*., 2013; *Kessler et al*., 2005; *Lapham et al*., 2008; *Mau et al*., 2007] and even hypothesized for the study area [*Lapham et al*., 2013], although possibly due to the lack of large earthquakes in the time-series, such a correlation could not be proven. *Lapham et al*. [2013] also discussed a possible tidal influence on fluid flow activation, but unfortunately the pore fluid sampling frequency did not allow resolving tidal cycles. Studies in other seep areas, however, do indicate gas flux variability related to tidal pressure with an indication of increasing flux during falling tidal pressure, e.g., at Coal Oil Point [*Boles et al*., 2001], Hydrate Ridge [*Tryon et al*., 1999; *Torres et al*., 2002], offshore Taiwan [*Hsu et al*., 2013], or Cape Lookout Bight [*Martens and Val Klump*, 1980].

In this study, we use long-term monitoring data of gas bubble observations by frequent sonar scans at a seep site off Vancouver Island in 1250 m water depth to (a) characterize the gas emission variability and (b) analyze the factors influencing its activity. By providing detailed long-term observations, we aim for more precise quantifications of total gas fluxes from the sediment to the ocean and, hence, better understand the significance of naturally driven hydrocarbon gas emissions. Further, the seafloor installations equipped with numerous sensors enable correlation of the methane flux variability with bottom pressure changes, which helps to elucidate the possible trigger mechanisms at the studied seep site. Our results from gas emissions offshore Vancouver Island might be transferred to similar seep sites and should provide a better understanding of controlling factors in such fluid systems.

### 1.1. Study Area

The Northern Cascadia continental margin offshore Vancouver Island is formed by the subduction of the Juan de Fuca Plate under the North American plate creating an accretionary prism (Figure 1a). In the course

of subduction, the sediments deposited on the incoming oceanic crust are accreted and furthermore folded and faulted forming elongated anticlinal ridges up to 700 m in height above adjacent basins [*Davis and Hyndman*, 1989]. Accretionary margins are usually prone to the occurrence of seafloor gas seepage and mud volcanism [e.g., *Kopf*, 2002; *Suess*, 2010]. Fluid flux is driven by the tectonic forces during the accretion process [e.g., *Hyndman et al*., 1993] and the degradation of organic matter often leads to a high amount of light hydrocarbons in the sediments within the prism. Offshore Vancouver Island, several areas of seeping fluids and free gas emissions are known and visually proven including the site investigated in this study near Bullseye Vent [e.g., *Riedel et al*., 2002, 2006a, 2010a] at the so-called Clayoquot Slope, which is located at a midslope basin in about 1250 m water depth and approximately 20 km landward of the deformation front. The evolution of fluid expulsion (cumulative volume as well as expulsion rate) from tectonic processes was first modeled by *Hyndman and Davis* [1992] for the accretionary prism off Vancouver Island and subsequently substantiated with pore-fluid data from drilling and coring based on Integrated Ocean Drilling Program (IODP) Expedition 311 [*Riedel et al*., 2010b]. The highest expulsion rate predicted is $\sim$2.5 mm yr$^{-1}$, and the largest signal in pore fluid expulsion in form of regional pore-water freshening was seen at $\sim$22 km from deformation front. Coincidentally, within a close range around this distance from the deformation front, a high number of cold seeps (in addition to Bullseye Vent), carbonate mounds, and gas flares are observed [e.g., *Riedel et al*., 2002; *He et al*., 2007; *Riedel et al*., 2010a; *Furlong*, 2013].

The margin is also characterized by abundant occurrences of gas hydrate, suggested by widespread observations of the seismically detected bottom-simulating reflector [e.g., *Hyndman and Spence*, 1992; *Yuan et al*., 1996] and proven from extended drilling and coring operations as part of Ocean Drilling Program (ODP) Leg 146 [*Westbrook et al*., 1994] and IODP Expedition 311 [*Riedel et al*., 2006b]. In a few areas gas hydrates were found also at shallow subseafloor depths, e.g., at Bullseye Vent [*Riedel et al*., 2006a, 2006b; *Lu et al*., 2005] or exposed on the seafloor at the Barkley Canyon site [e.g., *Spence et al*., 2001; *Chapman et al*., 2004; *Thomsen et al*., 2012], the latter being the only known area in Northern Cascadia of thermogenic gas and oil seepage [e.g., *Pohlman et al*., 2005]. Gas hydrates at Barkley Canyon occur as structure II as well as structure H [e.g., *Lu et al*., 2007].

The Cascadia Subduction Zone is characterized by a potentially fully locked seismogenic zone where very large thrust earthquakes can occur but currently only little seismicity on the main thrust plane is observed [*Hyndman and Wang*, 1993; *Obana et al*., 2015]. Paleoseismic data from the margins of southern British Columbia, Washington, and Oregon indicating abrupt vertical motion and shaking in coastal regions [*Clague*, 1997; *Hyndman and Rogers*, 2010] and analyses of simultaneous turbidite flows in several deep-sea channels were interpreted that major earthquakes did occur on the northern Cascadia margin in irregular intervals averaging 500–530 years [*Goldfinger et al*., 2012]. The most recent megathrust earthquake occurred in 1700 [e.g., *Hyndman and Wang*, 1995; *Clague and Bobrowsky*, 1994; *Atwater et al*., 1995; *Satake et al*., 1996; *Goldfinger et al*., 2003; *McAdoo et al*., 2004]. However, the Cascadia subduction zone lacks widespread earthquakes in the forearc region and in the subducting Juan de Fuca Plate [*McCrory et al*., 2012; *Obana et al*., 2015], which is also revealed by only minor earthquake detections during the 13 month of our study (Figure 1a). In contrast, numerous earthquakes have been recorded along the offshore ridge-fracture zone system, both the divergent and transform segments. Additional main earthquake centers are at the Queen Charlotte fault system (north of subducting Explorer Plate), along the Nootka Fault (separating the Explorer and Juan de Fuca Plates) and at the Mendocino triple junction (the juncture of three plate-bounding faults: the Mendocino transform fault, the Cascadia subduction zone, and the San Andreas fault).

## 2. Methods

Ocean Networks Canada's North-East Pacific Time Series Underwater Networked Experiments (NEPTUNE) cabled ocean observatory [*Barnes et al*., 2011] enables nondestructive, controlled experiments, and time-series observations integrating numerous sensor's recording data in several areas of scientifically high interest offshore Vancouver Island (Figure 1a). One of the five nodes of the NEPTUNE cabled observatory connecting various instruments is installed at Clayoquot Slope (Figure 1b) with the purpose of monitoring the fluid system in a setting with the margin's highest fluid expulsion rates influenced by tectonic forces. Data storage, retrieval, and delivery are managed by the Ocean Networks Canada's Oceans 2.0 system and data are made readily accessible for the public through the internet.

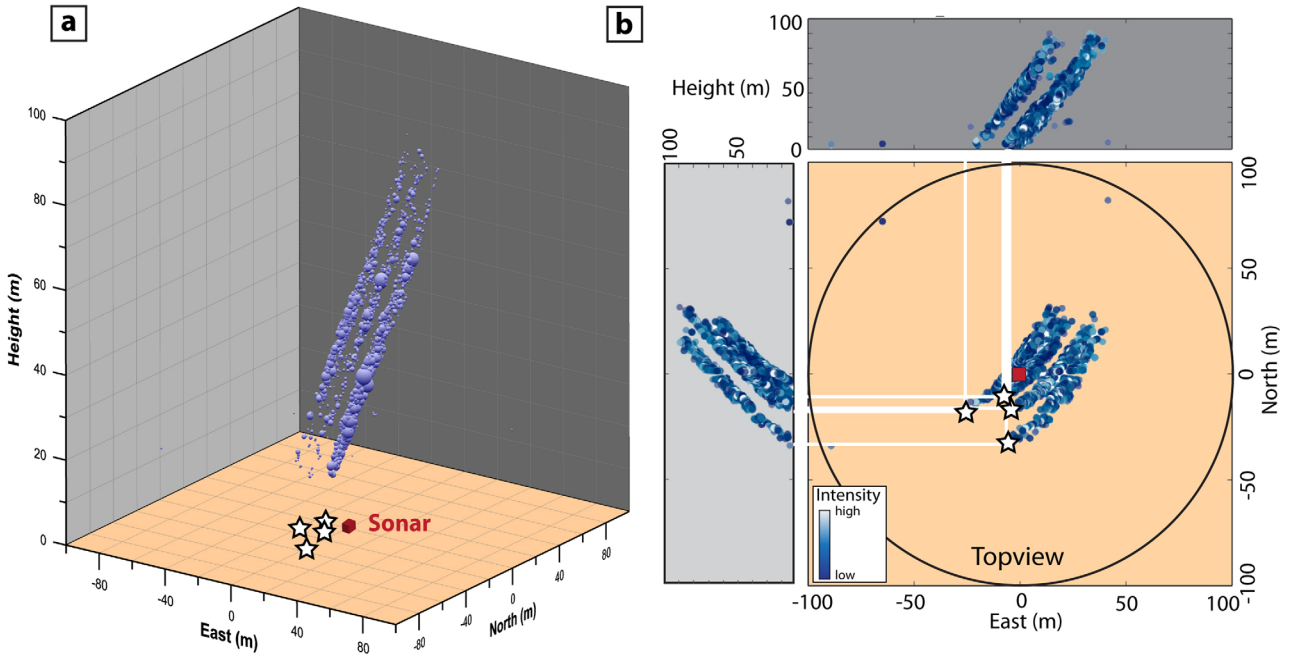


**Figure 2.** Visualization of sonar data showing extracted flares in (a) a 3-D-plot and (b) a combined 2-D-plot allowing for detecting source locations of emanating gas bubbles (white stars).

### 2.1. Sonar

Monitoring the gas bubble emissions from the seafloor into the water column is enabled by a rotating IMAGENEX Model 837B Delta T multibeam profiling sonar installed in combination with an 837 Delta T Azimuth Drive. The sonar operates at a frequency of 260 kHz and set to the maximum range of 100 m. The transducer beam width is 120° × 3° (vertical and horizontal, respectively) and a rotation of 360° is achieved after 120 pings with clockwise rotating steps of 3°, which takes about 2 min per sweep, and stored in a manufacturer's raw file. Besides the strong reflection of the seafloor, free gas in the water column also strongly enhances the received backscatter signal, and vertically rising gas bubble emissions are therefore clearly imaged in the records. To further analyze the raw data, processing steps like e.g., beam-forming and time-variant gain were applied. The data were then filtered to remove some noise on the central channels, to cut the vertically projecting sector, and to isolate the free gas reflections, to finally (a) image the records in a 2-dimensional or 3-dimensional plot (Figures 2a and 2b, respectively), and (b) produce time-series by extracting information of the activity of the gas emissions. In a simple approach, any presence of a gas bubble stream was detected manually and plotted as events of activity over time. Furthermore, in a semiquantitative approach, the mean value of the received backscatter intensity was calculated for each scan and plotted against a timeline. A challenge in the analysis is the presence of nonbubble backscatter resulting from e.g., fish, large plankton, and detrital particles as described by *DelSontro et al*. [2015] and *Scandella et al*. [2016]. Our visual inspection does allow for a relatively reliable distinction between bubbles and nonbubble targets; however, they had to be neglected for the automatized mean sonar backscatter calculation.

Data gaps result from failures of the instrument, either due to entire breakdown for five weeks in autumn 2012 or due to stagnancies of the rotating device, which happened two times each lasting ∼2 weeks in spring 2013.

### 2.2. Additional Sensor Data for Time-Series Analyses

A variety of installations are connected to the NEPTUNE node at Clayoquot Slope (Figure 1b), enabling simultaneous records at the same study site for comprehensive analysis and comparisons. For this study, time-series data of (a) the bottom pressure recorder (BPR), (b) the current meter, (c) the conductivity-temperature-depth (CTD) sensor, and (d) the seismometer were extracted (supporting information Table S1). The seafloor pressure (in decibar) from the BPR, as indicator for the tide information, was down sampled to one minute and 10 min for statistical analyses and to 1 h for overview plots. Spectrograms for pressure were generated for illustration of storm periods and earthquake events [see *Davis and Heesemann*, 2015].

One hour averages were also downloaded for the current speed (in m/s) from the Nortek Aquadopp Current Meter and the temperature data (in °C) from the CTD (Sea-Bird Microcat SBE37SIP). Data from the broadband seismometer (Guralp CMG-IT Broadband Seismometer) were condensed to Real time Seismic Amplitude Measurement (RSAM; *Endo and Murray* [1991]) data averages; the vertically orientated component (LHZ or MHZ) were downloaded from the Incorporated Research Institutions for Seismology (IRIS) and averaged to once per minute.

Information about sea surface wave heights were derived from nearby Buoy 46206 data downloaded from the Fisheries and Oceans Canada website (http://www.meds-sdmm.dfo-mpo.gc.ca/isdm-gdsi/waves-vagues/search-recherche/list-liste/data-donnees-eng.asp?medsid=C46206), and the characteristic wave height, calculated from low frequency cut-off to maximum frequency (VCAR), was chosen for comparative time-series plots. Earthquake events (local, as well as teleseismic) were exported both from the IRIS earthquake browser (www.iris.edu/ieb), and from the website of the Natural Resources Canada earthquake catalog (http://earthquakescanada.nrcan.gc.ca/stndon/NEDB-BNDS/bull-en.php).

### 2.3. Hydroacoustic Systems

Hydroacoustic data including multibeam and single beam echosounder records were collected during several expeditions with research vessels to the study area of Clayoquot Slope. Water column anomalies visible in single beam echosounder data collected before 2010 were analyzed by *Zyla* [2011] and *Riedel et al*. [2010a]. The data collection by *Zyla* [2011] includes flare locations detected by a horizontally looking sonar mounted on the ROV Doc Ricketts from the Monterey Bay Aquarium Research Institute (MBARI) deployed during an expedition with the Western Flyer in 2009 [see *Furlong*, 2013]. Additional information of flare occurrences were collected during a cruise with R/V Tully in September 2010 [*Riedel et al*., 2014; *Whiticar et al*., 2010] and, most recently, in May 2014 using an EK60 split beam echosounder operating with frequencies of 18, 38, 70, 120, and 200 kHz. However, flares became best visible at the lower frequencies due to resonance frequency of the emanating bubbles in that water depth, and therefore the 18 kHz signal was analyzed for this study. Multibeam data were recorded during a cruise with R/V Falkor in September 2013 using a Kongsberg EM710 which, in addition to the information of the bathymetry, also records backscatter intensities in the water column allowing for flare detection. RAW data of the single beam and multibeam systems were imported into QPS Fledermaus Midwater Tool, and after a simple processing enhancing the contrast, exported as sd-format files to be opened together with the bathymetric data in the 3-D Fledermaus software.

In addition, the AUV *D. Allan B*. owned by MBARI was deployed at Clayoquot Slope in May 2009 during a research expedition on R/V Zephyr [see e.g., *Furlong*, 2013]. The AUV was equipped with a single beam echosounder Edgetech 2–15 kHz chirp subbottom profiler for imaging subseafloor structures and a RESON 7215 multibeam echosounder (operating at 200 kHz) providing high-resolution bathymetric data with ~1 m lateral resolution and also flare information within the water column record by data processing with CARIS Hips and Sips.

## 3. Results

### 3.1. Hydroacoustic Observations at Clayoquot Slope

At Clayoquot Slope, several flares have been detected hydroacoustically during research expeditions to the study area between 2006 and 2014. Although a systematic flare mapping of the entire area was lacking until now (with the exception of the early map shown by *Riedel et al*. [2010a]), the main seep sites were already identified using high-resolution seismic techniques in 1997 [*Gettrust et al*., 1999] and subsequently confirmed using 3-D imaging techniques [*Riedel et al*., 2002]. The first recognition and digital recording of gas flares were made in 2006 [*Willoughby et al*., 2008]. Prior to the R/V Falkor cruise in 2013, the water column was surveyed using single beam echosounders with a relatively small footprint (of about 7% the water depth) in contrast to multibeam systems. Therefore, gas emissions located as close together as the footprint of the echosounder appear as connected backscatter anomalies and cannot be distinguished. However, the records provide an overview of the seep sites and show that at a few sites, flares have been frequently observed whereas at a few other sites such anomalies could be detected only once (Figure 1b). The main seep sites were informally named Gastown Alley, where several flares are aligned in a SW-NE direction, and Bubbly Gulch, a region in the NE sector of the study area, where several flares occur associated with a submarine slope failure that exposed gas-charged sedimentary layers, resulting in the formation of several

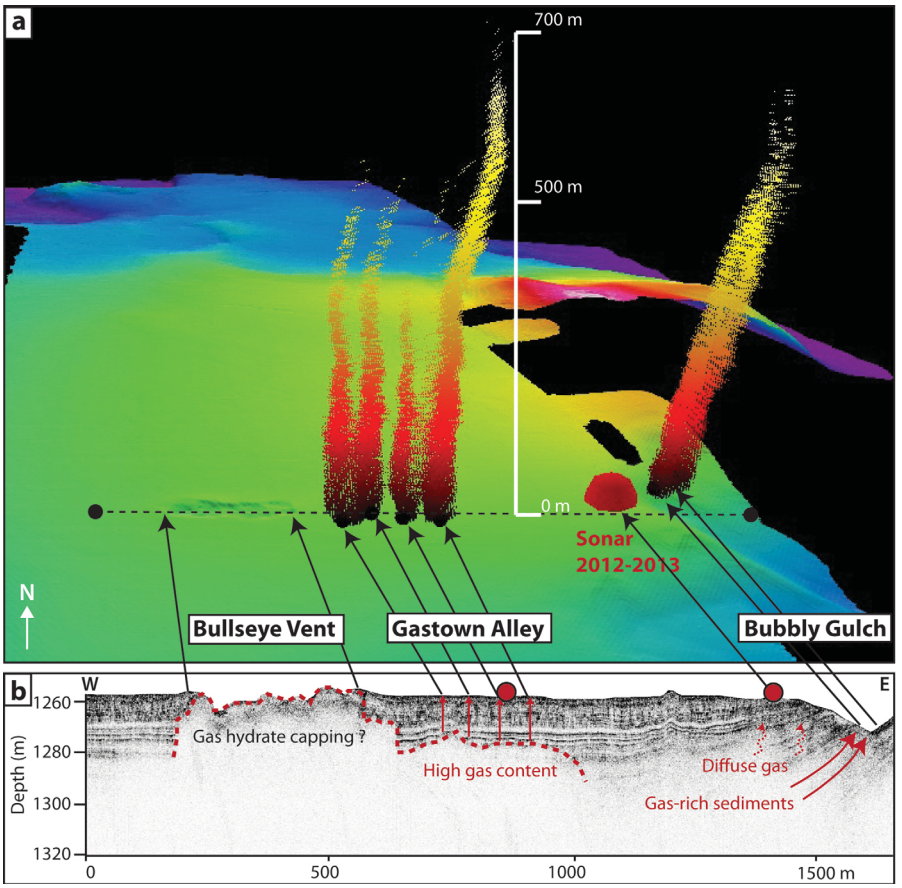


**Figure 3.** (a) 3-D plot showing a high-resolution bathymetric grid recorded by AUV Sentry in 2009 plotted together with flares extracted from ship-based multibeam data in 2013 and the sonar position (symbolized by a red dome resulting from the detection limit). Flares aligned in Gastown Alley and Bubbly Gulch reach 700 m in height. (b) Subbottom profile recorded with the AUV Sentry indicates diffuse blanked zones related to gas hydrate occurrences at Bullseye Vent and gas accumulated in the sediments below Gastown Alley and migrating along sediment layers toward Bubbly Gulch.

small seafloor domes hosting free gas and gas hydrate [e.g., *Paull et al*., 2009; *Furlong*, 2013]. Although forming a conspicuous morphological depression at the seafloor with massive underlying gas hydrate layers up to 50 m below seafloor [*Riedel et al*., 2006a] and widespread carbonate crusts [*Riedel et al*., 2002], no gas emissions were detected at the so called Bullseye Vent structure.

The flares detected with the ship-based echosounders appear different in intensities and heights, however, both parameters are dependent on the geometry of the vessel track to the flare locations and the quality of the records when using the single beam echosounder. Nevertheless, the multibeam records collected in 2013 indicated the presence of at least six flares with obvious differences in height as well (Figure 3a). Flare heights ranged between 500 and 700 m from the seafloor into the water column, the highest one disappeared in about 550 m below sea level (mbsl) at approximately the upper limit of the gas hydrate stability zone.

In the subbottom echogram imaging the sediment structures below Bullseye Vent, Gastown Alley, and Bubbly Gulch, the presence of enhanced gas content and possible migration pathways to the sea surface become visible (Figure 3b). The subbottom profile shows the generally horizontally layered sediments of the first ~30 m below sea floor (mbsf). However, below the prominent Bullseye Vent structure the strata is obscured, probably resulting from shallow gas hydrate presence as revealed by prior seismic interpretation and sediment coring [*Riedel et al*., 2006a] as well as authigenic carbonate precipitations. A similar blanking effect is also visible below Gastown Alley, but in contrast to Bullseye Vent in greater depth of approximately 20 mbsf. Due to the fact that intense flares are aligned at the seafloor on top (Figure 3a), we assume that the blanking is the result of enhanced gas and/or gas hydrate content in that area and gas migrated from this shallow reservoir

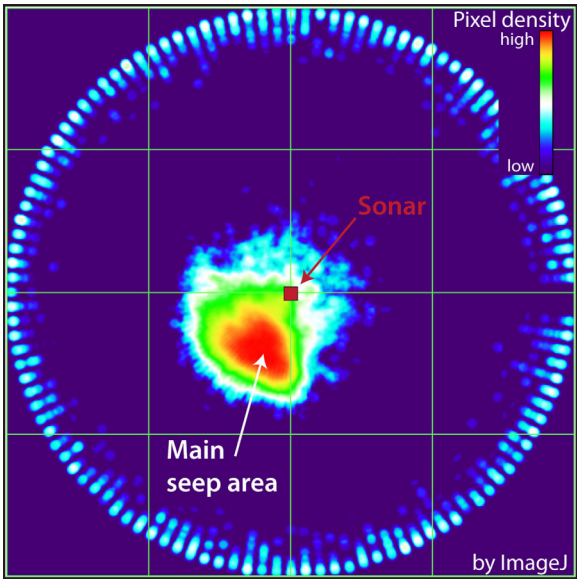


**Figure 4.** Heat map of flare sources indicates a main seep area located south and west of the sonar. Image created with ImageJ plugin "Heat-Map From Stack" by Samuel Pean.

vertically through the sediment strata to the surface where it emanates into the water column. Some diffuse blanking is also apparent below the sonar installation and Bubbly Gulch. Here, however, the sediment strata appear slightly bent upward and truncated by the depression. Gas is probably channeled mainly along the strata and fuel the flares detected within the depression of Bubbly Gulch (Figures 3a and 3b).

### 3.2. Gas Emission Activity

#### 3.2.1. 1 Year Time Series at Transient Flares With 1 h Interval

Between June 2012 and July 2013, the sonar records show phases of activity and inactivity in diverse variability patterns. Bubble streams become visible in the scanned hemisphere when rising vertically or most often deflected by currents. Depending on the distance of the gas source to the installed sonar and the direction of the current, the streams are displayed as linear anomalies of up to 100 m. Most often, single streams can be distinguished, however, if several streams emanated in a small area, the resolution may not be high enough to visualize them separately and the emission appears as a wide column or cloud. In various examples, bubbles emanate also in pulses, which is visible in the sonar records as elongated anomalies not attached to the seafloor. The amount of bubble streams highly vary between one individual to a few ($<5$) active streams at the same time. The source locations of the detected bubble streams at the seafloor have been plotted in order to visualize the distribution pattern. The result presented in a heatmap indicates a main seep area just southwest of the sonar position with a dimension of $\sim 40 \times 70$ m (Figure 4). Besides this main seep area, some orifices have been also detected northwest at larger distances ($\sim$70–120 m) to the sonar position and just a few bubble streams appeared in other areas; however, all of these secondary streams have been active only a few times and therefore do not appear on the heatmap.

In a first approach to analyze the variability of the gas emissions in the scanned hemisphere, the images produced for each hour were inspected manually for the presence of anomalies representing bubble streams (multiple high-backscatter reflections with a roughly vertical alignment). Times at which active gas expulsion could be determined were plotted over time in form of a bar chart with grey areas marking manually-identified activity periods as shown in Figure 5. During one year of observations, different generic phases of gas emission activity occurred. The first three months starting from June to end of August 2012 were characterized by about equally active and inactive time periods, each lasting between hours to several days. The following months almost until end of 2012 showed mostly active gas emission, interrupted by a few brief periods of inactivity ($<6$ h). The last 7 months of the record until mid of July 2013 was dominated by inactivity, but with frequently active time periods lasting only a few hours.

#### 3.2.2. Short-Term Variability of Gas Emissions

In addition to the simple illustration of active and inactive time periods of gas emission in a bar chart, we calculated the mean sonar backscatter intensities of each sonar scan allowing for a semiquantitative measure (in relative counts due to the uncalibrated sonar) of the bubbles emitted. Scans including gas bubble streams show elevated values whereas those without range in a certain interval (between 0.125 and 0.135), the mean background from seafloor backscatter and noise. Phases with considerable deviating mean background values indicate a malfunction of the rotational device of the sonar head, as happened twice in March and May 2013, respectively (marked therefore also as gaps in Figure 5). The slightly inclined seafloor morphology, which is partly recognized in the sonar records, is most probably the reason for the deviant mean sonar backscatter intensities. By comparing the automatized mean sonar backscatter intensities with the manually identified bubble ebullition activity phases several observations have been made:

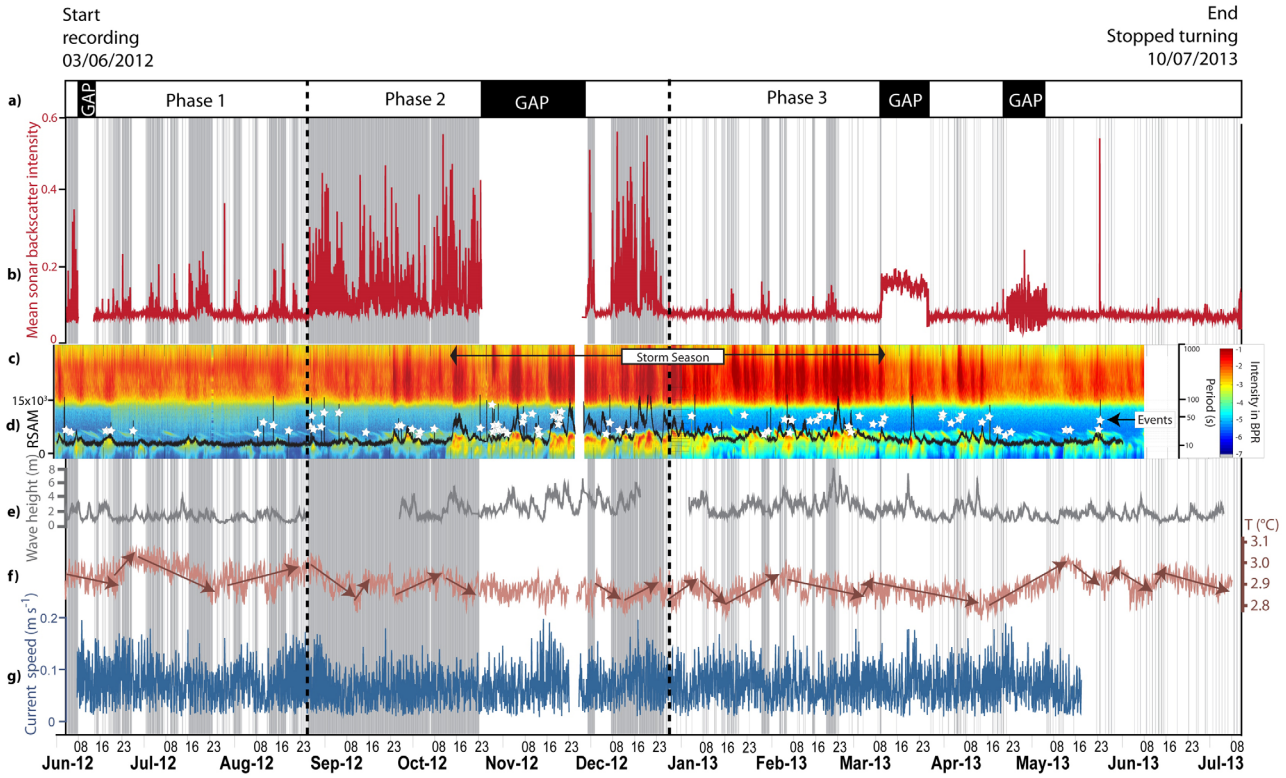


**Figure 5.** Time series plot over 13 month combining data of gas bubble activity, bottom pressure records, real-time seismic amplitude measurement (RSAM), wave height, bottom water temperature, and current speed. Indicated data gaps refer to malfunction of the sonar recording.

1. Elevated mean sonar backscatter intensities correspond with very few exceptions to activity phases, confirming a direct relationship. Some short activity phases as during Phase 3, with visually identified very minor flare activity, do not show elevated mean backscatter values (Figure 6c), indicating the limited detectability in the intensity data.
2. Mean sonar backscatter intensities during a single activity phase continuously increase until a maximum and subsequently decrease continuously without many runaway values or spikes (Figure 6c) that would indicate a fluctuating subpattern or a major bias by the 1 h scanning interval due to unresolvable flux heterogeneities. Both, decrease and increase take about the same time of roughly 3 h each.
3. During activity phases lasting longer than about half a day, e.g., during Phase 1 and 2 (Figures 6a and 6b, respectively), the mean sonar backscatter intensities indicate repeated sequences of increasing and decreasing gas emission activity.
4. A dominant period of 12.4 h was identified by analyzing the mean backscatter values using Fourier transformation (supporting information Figure S1). This result is identical to the period of the principle lunar semidiurnal M2 tidal component. The signal is less apparent in Phase 3 during which gas escape was weakest and active ebullition periods occurred less often.

### 3.3. Seismic Events Related to Gas Emission Activity

Analyses of the impact of earthquake events on the seafloor sediments at Clayoquot Slope have shown that various events even from distances >500 km and also teleseismic events could be recognized in RSAM ground shaking and in the bottom pressure records. In total, 70 abrupt high-intensity anomalies were detected between June 2012 and July 2013 in the data of the RSAM and 79 anomalies have been marked in the spectrogram for pressure (Events in Figure 5). About 90% of the anomalies in the RSAM seismometer shaking data correspond to events observed in the bottom pressure records. The same percentage of events in the BPR data (~90%) correspond to an anomaly, when the seismometer showed evidence for ground shaking, which might be caused by earthquakes. In order to analyze this dependence, all earthquake events documented for the same time period and sourced within the area of the Juan de Fuca and

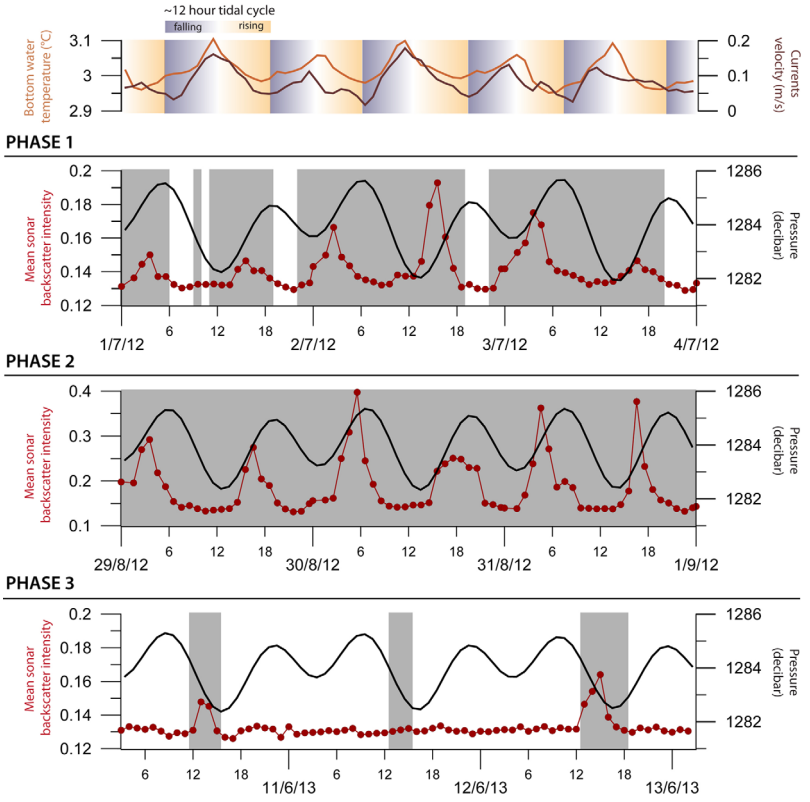


**Figure 6.** Excerpts of 3 days for each phase illustrating the relationship between mean sonar backscatter intensity (red) with the tidal pressure curve (black line). Bottom water temperature (yellow line) and current velocity (brown line) show a typical negative correlation with the tidal cycle.

Explorer Plates were used. The result illustrates that >50% of all events in the BPR can be explained by an earthquake. Those earthquakes being recognized at Clayoquot Slope in the RSAM (and BPR) data were further marked in the map (supporting information Figure S2). The earthquake locations are scattered along all plate boundaries around the Juan de Fuca and Explorer Plates, sourced either from the subduction zone, transform faults, or along the mid ocean ridge. The distances from the study area to the earthquakes recognized are up to ~650 km (supporting information Table S2). However, the IRIS database gives evidence for 595 earthquakes in the time period, out of which just 60 (~10%) possibly caused ground shaking at Clayoquot slope. Most earthquakes recorded at the sonar site on the seismometer and BPR occur at an azimuth of ~140° (measured relative to the sonar's position, supporting information Figure S3) with distances ranging from a minimum of 88 km to a maximum of 1050 km for local events originating at the Juan de Fuca plate system. Teleseismic events seen in the RSAM and BPR records are from as far as 9934 km. Magnitudes for the local events range from Mw = 2.2 to Mw = 7.8.

An example in Figure 7 shows a time-series plot over 14 days in August 2012: six anomalies were recorded in the RSAM, five of them become also visible in the BPR spectrogram, and also five anomalies can be correlated to earthquakes documented in the IRIS database. However, six further earthquakes occurred during this time period but have no effect in the BPR or RSAM record. Nevertheless, neither events in RSAM nor earthquake events occurred at the same time as an onset of gas emission activity. This example is not shown as an exception, rather as the norm; over the entire time period of ~13 month of the 595 earthquakes documented in the IRIS database just five occurred simultaneously to an onset of flare activity seen in the sonar records. Similarly, the 70 anomalies detected in the RSAM time-series over the entire 13 month, only one event was seen together with an onset of gas emission activity.

### 3.4. Oceanographic Conditions

#### 3.4.1. Seasonal Changes

The duration of the winter storm season in the study area offshore Vancouver Island can be illustrated best using the power spectrum of the BPR record (Figure 5c), in which the intensities are illustrated by different

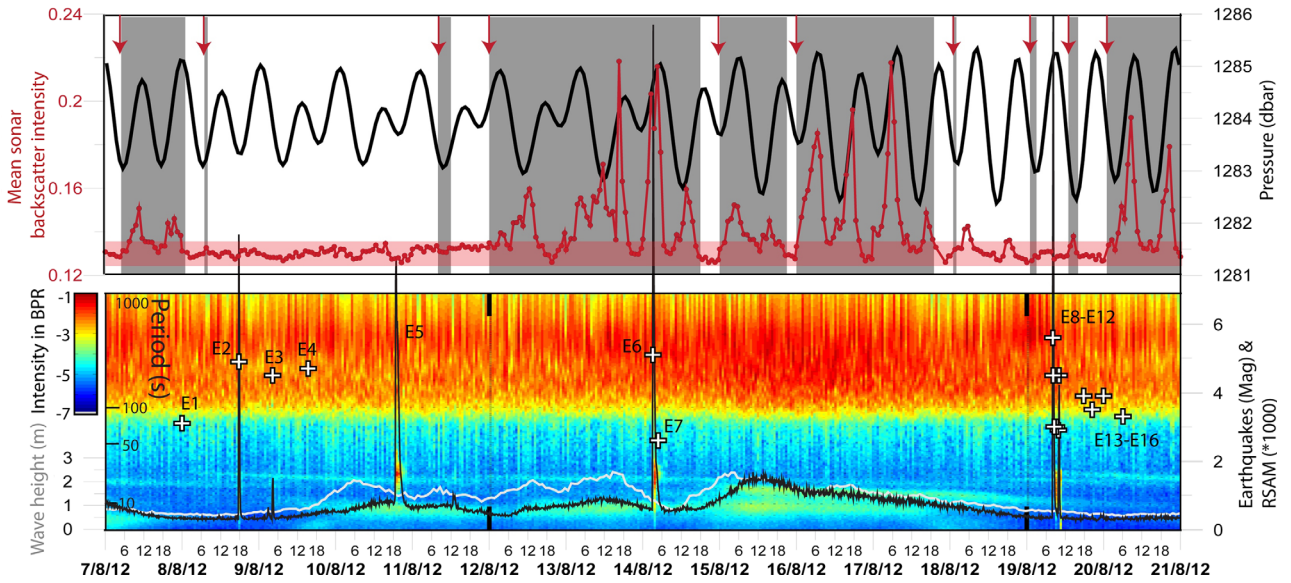


**Figure 7.** Details of the time-series analyzed (2 weeks in August 2012) focusing on the gas emission activation (red arrows) in relation to bottom pressure, wave height, RSAM, and earthquake events.

colors and plotted for periods between 1 and 1000 s on the *y* axis. The intensities both in long and short periods were frequently elevated in the timespan between October 2012 and March 2013 (Figure 5c), coinciding with increasing wave heights up to a maximum of over 8 m in February 2013 (Figure 5e) and also increased seismic amplitudes measured and plotted as RSAM time-series (Figure 5d). This relationship becomes especially visible focusing on the long periods in the BPR power spectrum, where yellow and red colors (illustrating high intensities) are generally accompanied by peaks in the RSAM and wave height values and concentrated in the winter months.

Bottom water temperatures between June 2012 and July 2013 ranged between 2.74 and 3.11°C with an average of 2.91°C over the ~13 months experiment (Figure 5f). The average value for the winter storm season (as defined above) is 2.89°C and slightly lower than during the other months that have a mean value of 2.92°C. The time-series further indicates trends lasting days to weeks (arrows in Figure 5f) that do not follow a frequent pattern. Finally, it appears that the temperature curve further shows a small-scale (<days) fluctuation that cannot be resolved with this overview plot.

Bottom water current magnitude values range between 0.01 and 0.20 m $s^{-1}$ with an average of 0.07 m $s^{-1}$ (Figure 5g) and the current direction indicates a slight dominance of the south-west (downslope) directed component. No obvious long-term trend has been recognized, but we observed small-scale (<days) fluctuations with amplitudes reflecting almost the entire range of the time-series.

### 3.4.2. Tidal Analyses

The bottom pressure variation recorded by the BPR at Clayoquot Slope can be 99.9% explained by the astronomic tide model used and the harmonic analysis results in the following main constituents: principal lunar semidiurnal M2 (40%), luni-solar declination diurnal K1 (18%), principal solar semidiurnal S2 (11%), lunar diurnal O1 (11%), larger lunar elliptic semidiurnal N2 (8%), solar diurnal P1 (6%), and others <6%. The Tidal form number (by calculating the amplitudes of O1+K1/M2+S2) of 0.58 indicates a mixed, mainly semidiurnal tidal regime. The M2 component is characterized by a period of 12.42 h equivalent to a frequency of 1.93 $d^{-1}$.

The mean bottom pressure value recorded during the analyzed timespan is 1284.0 dbar and range between 1281.7 and 1285.8 dbar. Average pressure values of the maximum and minimal turning points are 1285.0 dbar (standard deviation SD = 0.4) and 1283.0 dbar (SD = 0.5), respectively. Between turning points pressure falls and rises on average 1.9 dbar (SD = 0.8).

Besides the bottom pressure also the bottom water temperatures and the current magnitude records illustrate the tidal influence in the study area. Both data sets show a variation with the same frequency as the M2 tide as calculated for the bottom pressure records. Temperatures and current velocity curves are almost

parallel to each other and reverse to bottom pressure, e.g., maximum temperatures and highest current velocities coincide with low tides and vice versa (Figure 6).

## 4. Discussion

### 4.1. Trigger Factors for Gas Emission Activation

A major objective of this study was to examine and evaluate several different parameters possibly affecting gas emission activity. During the analyzed timespan of about 1 year the sonar records revealed 236 flare onsets, mainly occurring in Phases 1 and 3 when active and inactive periods alternate most often.

#### 4.1.1. Earthquake Shaking

One hypothesis was that earthquakes might affect subsurface fluid flow as a relation between methane release and earthquakes has been postulated already in several studies. *Mau et al*. [2007] measured an increase in bottom water methane concentrations offshore Chile after an earthquake in 2002. Another earthquake happening in the Gulf of Mexico was hypothesized to have caused an increase in methane from the sediment to the water column in an area with present gas hydrate deposits [*Lapham et al*., 2008]. *Fischer et al*. [2013] presented geochemical analyses of sediment cores from the Makran subduction zone, indicating a substantial increase in upward flux of gas dated to correlate with the strongest earthquake in the Arabian Sea in 1945. Also, hydroacoustically detected gas flares found in a tectonically active area in the Okhotsk Sea were related to have caused an increase in bottom water methane concentrations after the Neftegorsk earthquake in 1998 [*Obzhirov et al*., 2004]. A similar data set is shown from the Cariaco Basin where higher methane concentrations in the water column were assumed to be a result of a 1967 earthquake [*Kessler et al*., 2005]. The most reasonable explanation that earthquakes trigger gas emission is the creation of pathways for free gas to migrate easier through the sediments. Seismic shaking and exerting shear stress in the sediments result in fracturing and possibly gas ebullition.

Nevertheless, our study did not reveal any relation between gas emission activation and earthquake occurrences. Although we could illustrate that 79 of the earthquakes shown in Figure 1a have been recognized in the bottom pressure records and also resulted in abrupt movements of the surface sediments, only one of them happened approximately simultaneously to a flare onset. A similar result has been published by *Lapham et al*. [2013] that focus on studying diffuse methane flux measurements within Bubbly Gulch, located just ~300 m northeast of the sonar installation we analyzed here. Although the authors initially hypothesized that regional seismic activity may control the variable methane fluxes, they could not find a correlation between earthquakes and methane flux. They suspected that this lack of correlation might be explained by the minor magnitudes of earthquakes that occurred during the time series in their study, which would suggest a threshold level ($M \geq 4$) of earthquake activity that could trigger methane release. During our study, 13 earthquakes with magnitudes $M \geq 4$ and located less than 300 km in distance to the gas emission site were detected. Six of these earthquakes occurred during a data gap of the sonar record, limiting the number of events to seven available for an association to gas flares observations. Nevertheless, none of the seven earthquakes can be directly preceded to a flare onset. However, when considering the relationships between earthquake shaking and an onset of gas emission, a controlling factor is the azimuth between the source of shaking and the sonar-site. Certain earthquake's focal mechanisms may promote amplitude maxima (or minima) within the direction of the travel-path of the earthquake waves. Although a broad distribution of azimuths has been seen in the data set, the majority of earthquakes recognized ($>$ 75%) reached the sonar at an azimuth of around 140° (see supporting information Figure S2). Detailed analysis of the radiation pattern of P-, S-, and surface wave energy for each individual earthquake would need to be carried out if focal mechanisms were available, in order to identify whether the sonar-site at Clayoquot Slope is within the compressional or expansion lobe or even on a nodal plain of no motion. This may shed further light into the relationship of earthquake shaking and the ability to induce gas emission. Also, the sediment-filled basin around the sonar site [e.g., *Riedel et al*., 2002] may provide a shape that results in local amplification of ground motion from only certain frequencies and azimuths (i.e., resonance effects), similar to the response of buildings to earthquake shaking. The absence of any connection between earthquake shaking and gas emission may be explained by these geometric effects. However, the mostly small earthquakes detected in the time period of the sonar activity were too small for defining focal mechanisms and also may be simply too small in magnitude to induce significant ground motion to mobilize gas or even result in gas ebullition.

Additionally, the frequency of sonar measurement of one value per hour could limit the earthquake relationship analysis. If earthquake shaking induces a short-lived spike in bubble intensity, this would not necessarily be detectable in the data set. In supporting information Table S2, we used the TauP toolkit [*Crotwell et al*., 1999] to calculate the travel time for P- and S-waves (body waves) to reach the sonar site from the hypocenter for a standard reference Earth-model. The maximum delay is ∼2.3 min for P-waves, and ∼4 min for S-waves. Surface waves, with usually larger amplitudes but lower frequency content than body waves, traveling along the seafloor would be slower, roughly at half or one third of the speed of the body waves. This would increase the delay time of those values reported in supporting information Table S2 by a factor of 2–3; yet, this results in no more than ∼10 min delay for surface waves originating at local events around the Juan de Fuca plate. A possibility to detect short-lived fluctuations of bubble intensity from earthquake shaking is to increase sampling of the sonar immediately after a local earthquake is detected. Although detected by the seismometer, none of the earthquakes did seem to result in long-lasting increased gas emissions.

Linked to the question of earthquake-trigger mechanisms are long-term variations in the stress state of the subducting oceanic plate, as e.g., associated with episodic tremor and slip or ETS underneath Vancouver Island [e.g., *Dragert et al*., 2001; *Kao et al*., 2009]. Although at far distance to the offshore accretionary prism (∼100 km lateral), changes in the crustal stress can propagate updip and affect the accretionary prism [*Davis et al*., 2011]. Approximately 14 days after the onset of ETS at the Costa Rica margin, changes in borehole pressures were observed, indicating that the outer prism experienced contraction. Such mechanism could also contribute to changes within the stress state of the sediment column and thus may influence gas emissions on a broader scale. ETS occurs underneath Vancouver Island periodically with a recurrence interval of 14–16 months. During the time of our gas-emission record, ETS occurred between 30 August and 11 October 2012, with some first indication of tremor activity as early as 14 August 2012 (https://www.pnsn.org/tremor/tremor-log/ets-event-of-summer-2012). Approximately 10 days after the onset of ETS underneath Vancouver Island, the gas emission activity at Clayoquot changed significantly and remained high (Phase 3) from 23 August 2012 to 23 December 2012. However, whether there is a correlation between the onset of ETS and Phase 3 of our gas emission record cannot be proven from the data currently available.

#### 4.1.2. Oceanographic Variability

We observed not only short-term variations in gas emission activity in the order of a few hours to a few days, but also detected long-period changes lasting several months. Such changes, as described in the main three phases of activity, may be related to long-period variations of oceanographic conditions around the cold seep site. Several phenomena are known in the area of our study that could exert long-period changes to the environmental conditions affecting gas emission, including seasonal storms, seasonal upwelling, climate-phenomena such as El Niño, or Pacific decadal oscillations (PDO).

The west coast off Vancouver Island is affected by a seasonal change in storm activity, with the typical storm season lasting through the winter months from October to April. The storm activity is easily detected on the BPRs as additional pressure forcing (see e.g., Figure 5). The storms are associated with a large variation in surface wave heights, similar in magnitude to the tidal forcing, but associated with a much higher temporal frequency and shorter wavelengths. However, we did not notice a relation between gas emission activity to the entire period of winter storms or individual storm events.

Seasonal changes in the bottom temperature and bottom current conditions may be linked to the seasonal upwelling occurring on the West coast off Vancouver Island [e.g., *Thompson*, 1981]. During the upwelling events, cold and nutrient-rich water from intermediate-depths (100–300 m) reaches the surface and results in increased biological productivity in coastal regions. This upwelling and shift in near-surface oceanographic conditions typically occurs in the summer months (June–August) off Vancouver Island. Yet, during this period, we observed two different general activities of gas emissions (Figure 5): in June–August 2012, the system showed variable gas emission activity (Phase 1), whereas over the same period in 2013, no gas emission was seen (Phase 3). As upwelling is a dominantly wind-driven phenomenon, upwelling varies in strength [*Bylhouwer et al*., 2013] on annual to decadal time-scales. Such variation may also be linked to changes in surface-water temperature influenced by the Pacific Decadal Oscillation [*Mantua and Hare*, 2002] or other climate-phenomena such as El Niño [*Bylhouwer et al*., 2013]. However, our study is too short for any conclusive analysis on such long-period variations in oceanographic conditions off Vancouver Island but possible correlations cannot be excluded.

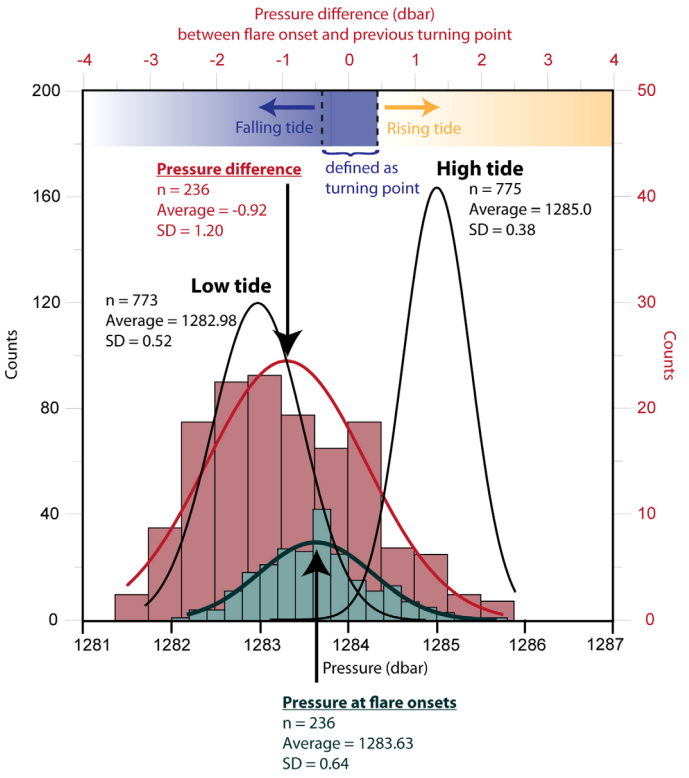


**Figure 8.** Histogram of the tidal analyses and flare onsets illustrating that the majority of flare onsets happen during falling tides close to low tide turning points.

### 4.1.3. Tidal Modulation

A correlation of the onset of gas emission activity was found to be with falling tides. Eighty-eight percent of all detected flare onsets (n = 236) happened between falling bottom pressure and low tide turning point (the latter defined as ±0.4 dbar pressure difference). The average pressure difference between flare onsets and the previous pressure turning point (high or low tide peaks) was −0.92 dbar (SD = 1.2) demonstrating the dominance of flare onsets during falling tides (Figure 8). Furthermore, the respective distribution of the correlating pressure values during the flare onsets is Gaussian shaped and mainly interfering with the curve of the low tide maxima pressure distribution, and with an average of 1283.63 dbar (SD = 0.64) rather in the lower pressure regime, i.e., closer to the low tide peaks than high tide peaks (Figure 8). Three examples of time series are shown in Figure 6 illustrating the gas emission activity (as grey-colored bars) in relation to the bottom pressure (black lines) over three days for each phase. Flare onsets are shown in Phases 1 and 3, all occurring during falling tides.

Observations of gas emission triggered by falling tidal pressure have been described in the literature earlier, mainly at very shallow marine and lacustrine environments. For example, *Boles et al.* [2001] showed with gas flux data over 9 months that marine seeps at Coal Oil Point in 67 m water depth are tidally controlled. Bubble ebullition at Cape Lookout Bight (North Carolina) is also assumed to be triggered by low-tide hydrostatic pressure release [*Martens and Val Klump*, 1980]. And in a recently published study by *Scandella et al.* [2016] the authors confirmed that bubble ebullition in Upper Mystic Lake (Massachusetts) is strongly episodic and largely controlled by hydrostatic pressure using the same multibeam sonar device we used in this study. *Scandella et al.* [2011] propose that methane transport in lake sediments is controlled by dynamic conduits, which dilate and release gas as the falling hydrostatic pressure and tested their model against a 4 month record of hydrostatic load and methane flux in Upper Mystic Lake. Shallow sites have often been the preferred in focus due to their easier accessibility and because methane fluxes from shallow sites are more favorable to contribute to the atmospheric methane inventory. In order to evaluate the role of Siberian thaw lakes as a positive feedback effect on climate warming, *Walter et al.* [2006] also investigated the variability of methane fluxes and stated that methane ebullition was triggered by falling hydrostatic pressure.

Nevertheless it has been proposed that tides have an influence also on seep sites at deep-water ocean settings, e.g., at Hydrate Ridge [*Torres et al.*, 2002; *Tryon et al.*, 1999] based on intermittent observations. *Kannberg et al.* [2013] could image flare intensity during repeated surveys, thus prolonging the observation timespan, but the results seemed not to correlate with tides, beside some bubble burst occurring during falling tides. They therefore suggested that even longer time series are needed to resolve the question whether tides are the primary factor modulating the bubble flux at Hydrate ridge.

### 4.2. Gas Emission Intensity During A Tidal Cycle

At Clayoquot Slope, not only gas emission activation seems to be controlled by the tidal pressure but also the emission intensity. Analyzing the flare intensity time series resulted a period of 12.4 h, which is identical

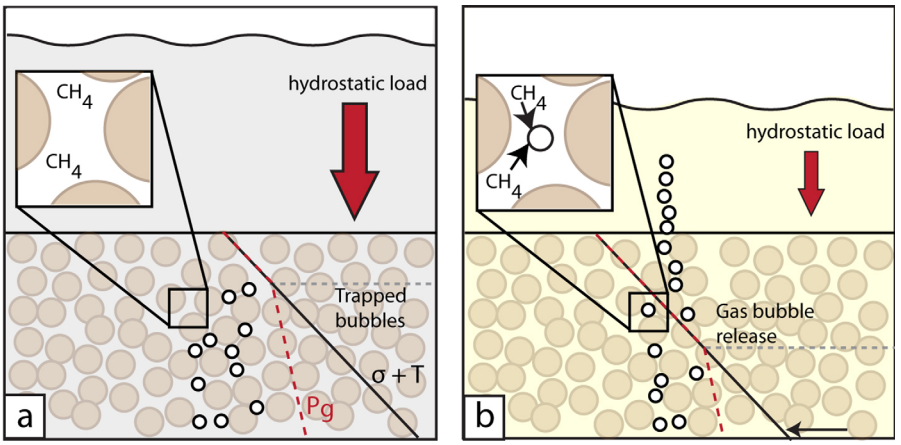


**Figure 9.** Schematic view of the two main processes affecting the gas activity during the falling tidal pressure. (a) Hydrostatic load ($\sigma$) and effective tensile strength (T) are larger than the gas pressure in the sediments. Sediments are saturated with methane. (b) Due to decreasing hydrostatic load, the sediment depth where gas pressure equals $\sigma + T$ increases and shallower bubbles are released into the water column. Simultaneously, solubility increase leading to exsolution and enrichment of gas bubbles in the pore space.

to the period of the dominant semidiurnal lunar tidal mode M2 and has been identified also in the BPR record available for this study. The results indicate that gas emission intensity varies also during periods of on-going gas escape as best observed in Phase 2 (Figure 6). Turning points of the mean backscatter values representing relative gas emission intensity correlate with decreasing bottom pressure and accordingly falling tides. Similar to flare onsets during periods of alternating activity, bubble emissions start slowly to increase when pressure is lowest until a certain pressure value is reached during subsequent rising tide.

The main reason for bubble ebullition is thought to be the hydrostatic pressure variation during the tidal cycle. A hydrostatic pressure drop means that the total load on the bubbles decreases and that the total internal bubble pressure might become greater than the sum of the total load and the fracture resistance of the sediment, which would result in migrating bubbles though fracturing [*Boudreau*, 2012]. Although *Boudreau* [2012] admittedly do not believe that pressure changes have a major effect on formation of the initial bubbles in sediments, hydrostatic pressure drops seem to facilitate subsequent bubble flux, i.e., by reopening preexisting bubble conduits [*Scandella et al*., 2011]. The model presented by *Scandella et al*. [2011] illustrates the relation of water level drop and the depth of active gas bubble activation through conduits. Gas bubbles trapped in the shallow sediments are frequently released down to a certain depth that is dependent on the hydrostatic tidal pressure (Figure 9). Gas is released when the gas pressure (Pg) equals the vertical stress ($\sigma$, by hydrostatic load and bulk sediment weight) together with the effective tensile strength (T, depending on the sediment composition and increasing with depth due to compaction). Tidally induced pore pressure changes has been further shown to be a function of depth and sediment composition and especially the presence of free gas effects tidally induced pore pressure variations and seafloor displacements [*Wang and Davies*, 1996; *Wang et al*., 1998]. Another unknown and complicating factor would be the formation and dissociation of gas hydrates in the shallow sediments due to uprising and temporarily trapped gas. Gas hydrate formation has been visually documented to form around the emanating bubbles when collected for sampling, but it could not be proven if hydrates form also within the shallow sediments in our study site around the sonar installation. However, in case of gas hydrate formation in sediments, we assume that a pressure decrease would facilitate their destabilization and therefore enhance the effect of increasing bubble ebullition starting at low tides.

An additional but probably minor contribution on the bubble flux variability could be bubble exsolution from the pore water influenced by changing pressure and temperature during the tidal cycle (Figure 9). The solubility of methane varies with the temperature and pressure changes that have been measured at Clayoquot Slope. Using the model by *Duan and Mau* [2006] provided online (http://models.kl-edi.ac.cn/models/ch4-sea/), we quantified the differences by taking the low tide and high tide pressure values and the typical temperature variation during the tidal cycle into account. The pressure difference of 2 dbar results in a shift of solubility of about 0.00018 mol $kg^{-1}$, and in combination with the increase of 0.1°C with falling tides, the

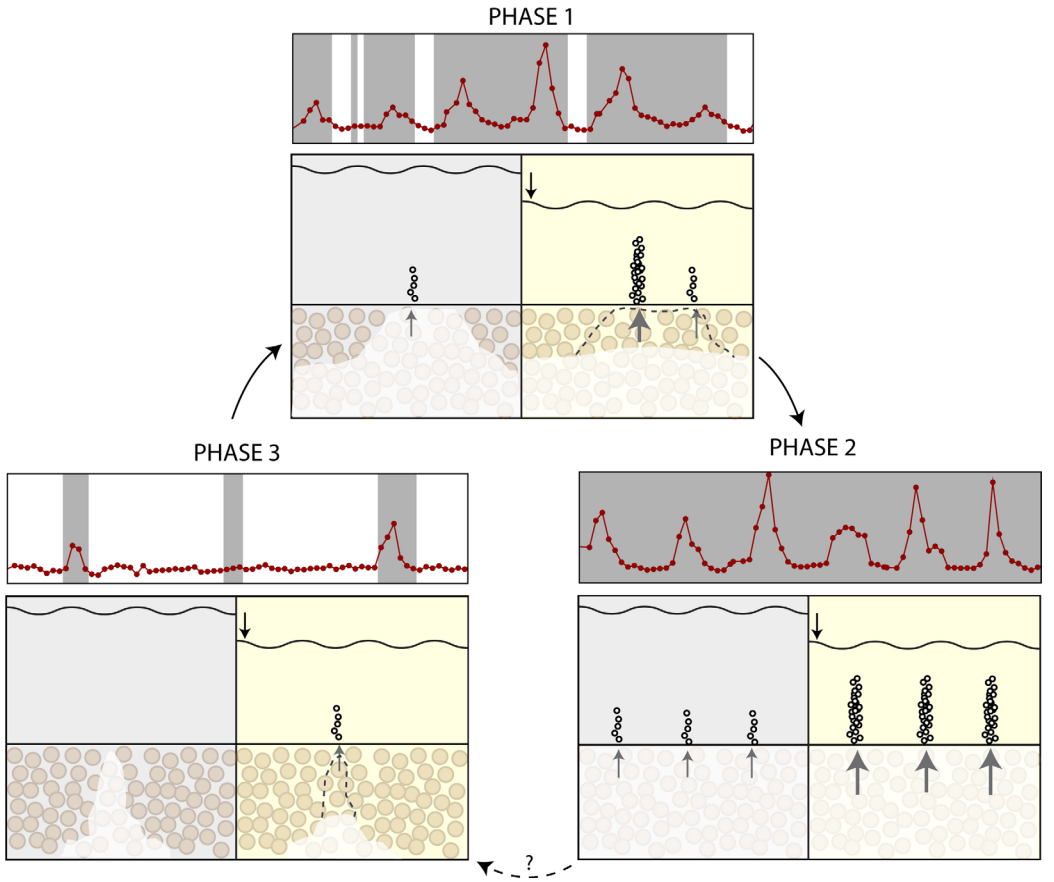


**Figure 10.** Schematic model of the long-term cycle of gas emission activity in relation to the three phases we defined from our data (example plots as shown in Figure 6) offshore Vancouver Island. Upward migrating methane fuels the pore space in the sediments (white shaded areas) and is frequently emitted into the hydrosphere in form of bubbles with intensities depending on the location within this cycle of phases.

difference in solubility amounts 0.0004 mol $kg^{-1}$. This value is probably rather an overestimation, as the temperature was measured in the bottom water and presumably reduced in the subsurface. *Lapham et al.* [2013] measured in the nearby Bubbly Gulch methane saturation values around 65 nM in the sediments. Subsequently, a 1 $m^2$of saturated sediment deposit would exsolve about 0.18 mol using the more conservative estimation (or 0.4 mol including the maximum temperature difference), which would equal around 30 mL methane as gas bubbles due to the tidal effect by assuming an impact down to 1 mbsf. Such a volume would be equal to ~170 gas bubbles of a typical bubble-size distribution. Even assuming a very weak gas bubble emission site, 170 bubbles would be released within seconds to minutes, but could not sustain continuous bubble streams over hours as visible in our sonar data. Although limited by simplification and assumptions, we hypothesize that the process of exsolution may contribute to, but not dominantly control the bubble flux variability observed at our study site at Clayoquot Slope.

### 4.3. A Variable Gas System At Clayoquot Slope

Our results of the gas emission time-series indicate three different phases of gas emission activity over 1 year. We hypothesize a general pattern of gas release controlled by various factors that include:

1. A steady connection of the gas reservoir with the subbottom and the absence of a shallow seal that could trap gas temporarily;
2. Constant microbial production rate of methane over short-time periods (hours to weeks) in the sediment column resulting in a steady source of gas;
3. Transient patterns, where the depth of gas mobilization is affected by pressure changes from short-period changes by tidal influences and just the very shallow subsurface is filling up with subsequent migrating gas between the tidal cycles;

4. Transient patterns from long-period changes (seasonal or decadal) of oceanographic conditions (e.g., PDO or upwelling) that mostly impact the temperature of the shallow subseafloor system and in turn may affect methane solubility and/or microbial activity; and
5. Transient patterns from long-period changes in tectonic forcing (e.g., ETS) that may contribute through additional gas migration from depth or by changing the stress state within the sediments.

A conceptual model is presented in Figure 10, illustrating a circle of the three different phases observed in our data. Phase 3 as the least active phase only emits gas bubbles for short-time periods during falling tides if already enough gas accumulated in the very shallow subsurface sediments. The more the subsurface becomes filled up with gas, the longer the active periods last (Phase 1). With on-going fueling, the active periods starting with falling tides do not empty the pore spaces of the shallow sediments until the next falling tidal stage, hence, gas bubbles are emitted (albeit with varying intensities) continuously (Phase 1 and 2). In Phase 2, the system is actively degassing throughout, until gas escape outpaces subsurface fueling and the circle starts over again with a transient pattern (Phase 3).

## 5. Conclusions

Observations of gas emission activity over 1 year at a cold seep site offshore Vancouver Island revealed a predominant tidal influence on seep activity. Analysis of the flare intensity time series resulted in a frequency identical to the semidiurnal lunar tidal mode M2. Furthermore, a coincidence of the onset of gas emission activity was found to be with falling tides when hydrostatic pressure decreases. We postulate a system for Clayoquot slope where gas emission is controlled on short time scales (hours to days) by tides, but also by long-period variations of the surrounding oceanographic regime (months to possibly years). Our 1 year observation shows that the same seep site can be either extremely active with almost continuous gas release, or very quiet with only minor short bursts of gas emissions. It shows that short-duration acoustic imaging from a research vessel, most likely yields a nonrepresentative snap shot of the entire system. Defining gas fluxes from such systems is therefore extremely challenging and although highly desirable, estimating a total carbon flux from the seafloor to the ocean at this (or any other) site is to be taken with caution and associated with a large uncertainty. The next increment of the long-term sonar installation within NEPTUNE, however, will allow for quantitative time series including absolute values as soon as additional data for calibrating the system is available. Our data presented in this study showing relative intensity time series, already indicate that gas flux estimates will vary by orders of magnitude depending whether the flux is defined during times of high activity (Phase 2) or overall low and/or intermittent activity (Phases 1 and 3).

Additional long-term monitoring at similar sites and for longer time periods are required to help reduce overall uncertainty in the question how much carbon is input to the world's ocean and thus may impact global questions such as ocean acidification or changes during ocean warming.

**Acknowledgments**

The writing of the paper was enabled by the kind invitation of the first author by Ocean Networks Canada (Kim Juniper) with a grant as visiting scientist for a close collaboration on analyzing the data from the NEPTUNE network. Furthermore, this research was primarily funded through the DFG-Research Center/Cluster of Excellence "The Ocean in the Earth System." We greatly appreciate the support by Charles K. Paull and Dave Caress for sharing bathymetric and subbottom data of AUV *D. Allan B.* (owned by MBARI) with us. Hydroacoustic data were acquired during several cruises between 2006 and 2014 on R/V Tully, R/V Thomsen, and R/V Falkor and we thank masters and crews for their professional assistance. Deployment and maintenance of the NEPTUNE instrumentation was successfully provided by the crew of ROV *ROPOS* (Canadian Scientific Submersible Facility). Time-series data from instruments installed within the NEPTUNE observatory are available through the Ocean Networks Canada Data search (http://dmas.uvic.ca/DataSearch) providing also links to the data derived from Fisheries and Oceans Canada and the Incorporated Research Institutions For Seismology (IRIS). We also thank Dietrich Lange at GEOMAR for the help in using TauP to calculate travel time delays for earthquakes detected in our data set. Finally, we want to thank two anonymous reviewers for their highly constructive comments that helped to significantly improve the manuscript.

## References

Atwater B. F., A. A. Nelson, J. J. Clague, G. A. Carver, D. K. Yamaguchi, and P. T. Bobrowsky (1995), Summary of coastal geologic evidence for past great earthquakes at the Cascadia subduction zone, *Earthquake Spectra*, *11*, 1–18.

Barnes, C. R., M. Best, F. R. Johnson, L. Pautet, and B. Pirenne (2011), Understanding Earth/ocean processes using real-time data from NEPTUNE Canada's widely distributed sensor networks, north-east Pacific, *Geosci. Can.*, *38*(1), 21–30.

Boles, J. R., J. F. Clark, I. Leifer, and L. Washburn (2001), Temporal variation in natural methane seep rate due to tides, Coal Oil Point area, California, *J. Geophys. Res.*, *106*(C11), 27,077–27,086.

Boudreau, B. P. (2012), The physics of bubbles in surficial, soft, cohesive sediments, *Mar. Pet. Geol.*, *38*(1), 1–18.

Bylhouwer, B., D. Ianson, and K. Kohfeld (2013), Changes in the onsset and intensity of wind driven upwelling and downwelling along the North American Pacific Coast, *J. Geophys. Res. Oceans*, *118*, 2565–2580, doi:10.1002/jgrc.20194.

Chapman, N. R., J. Pohlman, R. Coffin, J. Chanton, and L. Lapham (2004), Thermogenic gas hydrates in the northern Cascadia margin, *Eos Trans. AGU*, *85*(38), 361, doi:10.1029/2004EO380001.

Clague J. J. (1997), Evidence for large earthquakes at the Cascadia Subduction Zone, *Rev. Geophys.*, *35*(4), 439–460, doi:10.1029/97RG00222.

Clague J. J., and P. T. Bobrowsky (1994), Evidence for a large earthquake and tsunami 100-400 years ago on western Vancouver Island, British Columbia, *Quat. Res.*, *41*, 176–184.

Crotwell, H. P., T. J. Owens, and J. Ritsema (1999), The TauP Toolkit: Flexible seismic travel-time and ray-path utilities, *Seismol. Res. Lett.*, *70*, 154–160.

Davis, E. E., and M. Heesemann (2015), Resonant seismic and microseismic ground motion of the Cascadia subduction zone accretionary prism and implications for seismic velocity, *J. Geophys. Res. Solid Earth*, *120*, 993–1004, doi:10.1002/2014JB011644.

Davis E. E., and R. D. Hyndman (1989), Accretion and recent deformation of sediments along the northern Cascadia subduction zone, *Geol. Soc. Am. Bull.*, *101*, 1465–1480.
Davis, E., M. Heesemann, and K. Wang (2011), Evidence for episodic aseismic slip across the subduction seismogenic zone off Costa Rica: CORK borehole pressure observations at the subduction prism toe, *Earth Planet. Sci. Lett.*, *306*(3–4), 299–305.
DelSontro, T., D. F. McGinnis, B. Wehrli, and I. Ostrovsky (2015), Size does matter: Importance of large bubbles and small-scale hot spots for methane transport, *Environ. Sci. Technol.*, *49*, 1268–1276, doi:10.1021/es5054286.
Dragert, H., K. Wang, and T. S. James (2001), A silent slip event on the deeper Cascadia subduction interface, *Science*, *292*, 1525–1528, doi: 10.1126/science.1060152.
Duan Z. H., and S. D. Mao (2006), A thermodynamic model for calculating methane solubility, density and gas phase composition of methane-bearing aqueous fluids from 273 to 523 K and from 1 to 2000 bar, *Geochim. Cosmochim. Acta*, *70*(13), 3369–3386.
Endo, E. T., and T. Murray (1991), Real-time Seismic Amplitude Measurement (RSAM): A volcano monitoring and prediction tool, *Bull. Volcanol.*, *53*(7), 533–545.
Fechner-Levy, E. J., and H. F. Hemond (1996), Trapped methane volume and potential effects on methane ebullition in a northern peatland, *Limnol. Oceanogr.*, *41*, 1375–1383, doi:10.4319/lo.1996.41.7.1375.
Fischer, D., J. M. Mogollon, M. Strasser, T. Pape, G. Bohrmann, N. Fekete, V. Spiess, and S. Kasten (2013), Subduction zone earthquake as potential trigger of submarine hydrocarbon seepage, *Nat. Geosci.*, *6*(8), 647–651.
Furlong, J. (2013), Characteristic morphology, backscatter, and sub-seafloor structures of cold vents on the northern Cascadia margin from high-resolution autonomous underwater vehicle data, MSc thesis, 181 pp., Univ. of Victoria, Victoria, British Columbia, Canada.
Gettrust, J., W. Wood, D. Lindwall, R. Chapman, R. Walia, D. Hannay, G. Spence, K. Louden, R. MacDonald, and R. D. Hyndman (1999), New seismic study of deep sea gas hydrates results in greatly improved resolution, *Eos Trans. AGU*, *80*(38), 439–440, doi:10.1029/99EO00320.
Goldfinger, C., C. Hans Nelson, and J. E. Johnson (2003), Deep-water turbidites as Holocene earthquake proxies: The Cascadia subduction zone and Northern San Andreas Fault systems, *Ann. Geophys.*, *46*(5), 1169–1194.
Goldfinger, C., et al. (2012), Turbidite event history—Methods and implications for Holocene paleoseismicity of the Cascadia subduction zone, *U.S. Geol. Surv. Prof. Pap.*, *1661–F*, 170 pp. [Available at http://pubs.usgs.gov/pp/pp1661f/.]
Greinert, J., D. F. McGinnis, L. Naudts, P. Linke, and M. De Batist (2010), Atmospheric methane flux from bubbling seeps: Spatially extrapolated quantification from a Black Sea shelf area, *J. Geophys. Res.*, *115*, C01002, doi:10.1029/2009JC005381.
He, T., G. D. Spence, M. Riedel, R. D. Hyndman, and N. R. Chapman (2007), Fluid flow and origin of a carbonate mound offshore Vancouver Island: Seismic and heat flow constraints, *Mar. Geol.*, *239*(1-2), 83–98, doi:10.1016/j.margeo.2007.01.002.
Hsu, S.-K., S.-Y. Wang, Y.-C. Liao, T. F. Yang, S. Jan, J.-Y. Lin, and S.-C. Chen (2013), Tide-modulated gas emissions and tremors off SW Taiwan, *Earth Planet. Sci. Lett.*, *369-370*, 98–107.
Hyndman, R. D., and E. E. Davis (1992), A mechanism for the formation of methane hydrate and seafloor bottom-simulating reflectors by vertical fluid expulsion, *J. Geophys. Res.*, *97*(B5), 7025–7041.
Hyndman, R. D., and G. D. Spence (1992), A seismic study of methane hydrate marine bottom simulating reflectors, *J. Geophys. Res.*, *97*(B5), 6683–6698.
Hyndman, R. D., and K. Wang (1993), Thermal constraints on the zone of major thrust earthquake failure: The Cascadia subduction zone, *J. Geophys. Res.*, *98*(B2), 2039–2060.
Hyndman, R. D. and K. Wang (1995), Constraints on the zone of potential great earthquakes on the Cascadia subduction thrust from current deformation and the thermal regime, *J. Geophys. Res.*, *100*(B8), 15,373–15,392.
Hyndman, R. D., and G. C. Rogers (2010), Great earthquakes on Canada's west coast: A review, *Can. J. Earth Sci.*, *47*(5), 801–820.
Hyndman R. D., K. Wang, T. Yuan, and G. D. Spence (1993), Tectonic sediment thickening, fluid expulsion, and the thermal regime of subduction zone accretionary prisms: The Cascadia margin off Vancouver Island, *J. Geophys. Res.*, *98*(B12), 21,865–21,876.
Kannberg, P. K., A. M. Tréhu, S. D. Pierce, C. K. Paull, and D. W. Caress (2013), Temporal variation of methane flares in the ocean above Hydrate Ridge, Oregon, *Earth Planet. Sci. Lett.*, *368*, 33–42.
Kao, H., S.J. Shan, H. Dragert, G. Rogers (2009), Northern Cascadia episodic tremor and slip: A decade of tremor observations from 1997 to 2007, *J. Geophys. Res.*, *114*, B00A12, doi:10.1029/2008JB006046.
Kessler, J. D., W. S. Reeburgh, J. Southon, and R. Varela (2005), Fossil methane source dominates Cariaco Basin water column methane geochemistry, *Geophys. Res. Lett.*, *32*, L12609, doi:10.1029/2005GL022984.
Kopf, A. J. (2002), Significance of mud volcanism, *Rev. Geophys.*, *40*(2), 1005, doi:10.1029/2000RG000093.
Lapham, L., R. Wilson, M. Riedel, C. K. Paull, and M. E. Holmes (2013), Temporal variability on in situ methane concentrations in gas hydrate-bearing sediments near Bullseye Vent, Northern Cascadia Margin, *Geochem. Geophys. Geosyst.*, *14*, 2445–2459, doi:10.1002/ggge.20167.
Lapham, L. L., J.P. Chanton, C. S. Martens, P. D. Higley, H. W. Jannasch, and J. R. Woolsey (2008), Measuring long term changes in dissolved ion and gas concentrations and stable isotopes at a hydrate site: Mississippi Canyon 118, Gulf of Mexico, *Environ. Sci. Technol.*, *42*, 7368–7373.
Leifer, I., and J. Boles (2005), Turbine tent measurements of marine hydrocarbon seeps on subhourly timescales, *J. Geophys. Res.*, *110*, C01006, doi:10.1029/2003JC002207.
Leifer, I., and A. Judd (2015), The UK22/4b blowout 20 years on: Investigations of continuing methane emissions from sub-seabed to the atmosphere in a North Sea context, *Mar. Pet. Geol.*, *68*(Part B), 706–717.
Leifer, I., and R. K. Patro (2002), The bubble mechanism for methane transport from the shallow sea bed to the surface: A review and sensitivity study, *Cont. Shelf Res.*, *22*(16), 2409–2428.
Lu, H., I. Moudrakovski, M. Riedel, G. D. Spence, R. Dutrisac, J. Ripmeester, F. Wright, and S. D. Dallimore (2005), Occurrences and structural characterizations of gas hydrates associated with a cold vent field, offshore Vancouver Island, *J. Geophys. Res.*, *110*, B10204, doi:10.1029/2005JB003900.
Lu, H., Y.-T. Seo, J.-W. Lee, I. Moudrakovski, J. A. Ripmeester, N. R. Chapman, R. B. Coffin, G. Gardner, and J. Pohlman (2007), Complex gas hydrate from the Cascadia margin, *Nature*, *445*, 303–306, doi:10.1038/nature05463.
Mantua, N. J., and S. R. Hare (2002), The Pacific decadal oscillation, *J. Oceanogr.*, *58*(1), 35–44.
Martens, C. S., and J. Val Klump (1980), Biogeochemical cycling in an organic-rich coastal marine basin-I. Methane sediment-water exchange processes, *Geochim. Cosmochim. Acta*, *44*(3), 471–490.
Mau, S., G. Rehder, I. G. Arroyo, J. Gossler, and E. Suess (2007), Indications of a link between seismotectonics and CH4 release from seeps off Costa Rica, *Geochem. Geophys. Geosyst.*, *8, Q04003, doi*:10.1029/2006GC001326.
McAdoo B. G., M. K. Capone, and J. Minder (2004), Tsunami hazard from submarine landslides on the Oregon continental slope, *J. Mar. Geol.*, *203*, 235–245.
McCrory, P. A., J. L. Blair, F. Waldhauser, and D. H. Oppenheimer (2012), Juan de Fuca slab geometry and its relation to Wadati-Benioff zone seismicity, *J. Geophys. Res.*, *117*, B09306, doi:10.1029/2012JB009407.

McGinnis, D. F., J. Greinert, Y. Artemov, S. E. Beaubien, and A. Wüest (2006), Fate of rising methane bubbles in stratified waters: How much methane reaches the atmosphere, *J. Geophys. Res.*, *111*, *C09007, doi*:10.1029/2005JC003183.

Nikolovska, A., H. Sahling, and G. Bohrmann (2008), Hydroacoustic methodology for detection, localization, and quantification of gas bubbles rising from the seafloor at gas seeps from the eastern Black Sea, *Geochem. Geophys. Geosyst.*, *9*, Q10010, doi:10.1029/2008GC002118.

Obana, K., M. Scherwath, Y. Yamamoto, S. Kodaira, K. Wang, G. Spence, M. Riedel, and H. Kao (2015), Earthquake activity on northern Cascadia subduction zone off Vancouver Island revealed by Ocean Bottom Seismograph observations, *Bull. Seismol. Soc. Am.*, *105*(1), 489–495.

Obzhirov, A., R. Shakirov, A. Salyuk, E. Suess, N. Biebow, and A. Salomatin (2004), Relations between methane venting, geological structure and seismotectonics in the Okhotsk Sea, *Geo Mar. Lett.*, *24*, 135–139.

Paull, C. K., W. Ussler, W. D. Caress, H. Thomas, E. Lundsten, M. Riedel, and L. Lapham (2009), Seafloor manifestations of gas venting and near seafloor gas hydrate occurrences, Abstract OS23B-05 presented at 2009 Fall Meeting, AGU, San Francisco, Calif.

Pohlman, J. W., E. A. Canuel, N. R. Chapman, G. D. Spence, M. J. Whiticar, and R. B. Coffin (2005), The origin of thermogenic gas hydrates on the northern Cascadia Margin as inferred from isotopic (13C/12C and D/H) and molecular composition of hydrate and vent gas, *Org. Geochem.*, *36*(5), 703–716.

Riedel, M., R. D. Hyndman, G. D. Spence, and N. R. Chapman (2002), Seismic investigations of a vent field associated with gas hydrates, offshore Vancouver Island, *J. Geophys. Res.*, *107*(B9), 2200, doi:10.1029/2001.

Riedel, M., I. Novosel, G. D. Spence, R. D. Hyndman, R. N. Chapman, R. C. Solem, and T. Lewis (2006a), Geophysical and geochemical signatures associated with gas hydrate related venting at the North Cascadia margin, *GSA Bull.*, *118*(1-2), 23–38, doi:10.1130/B25720.1.

Riedel, M., T. S. Collett, M. J. Malone, and the Expedition 311 Scientists (2006b), *Proceedings of IODP*, vol. 311, Integrated Ocean Drill. Program Manage. Int., Inc., Washington, D. C., doi:10.2204/iodp.proc.311.2006.

Riedel, M., A. M. Trehu, and G. S. Spence (2010a), Characterizing the thermal regime of cold vents at the northern Cascadia margin from bottom-simulating reflector distributions, heat-probe measurements and borehole temperature data, *Mar. Geophys. Res.*, *31*(1), 1–16, doi:10.1007/s11001−010-9080-2.

Riedel, M., T. S. Collett, and M. Malone (2010b), Expedition 311 synthesis: Scientific findings, in *Proceedings of IODP*, *311*, edited by M. Riedel et al., Integrated Ocean Drill. Program Manage. Int., Inc., Washington, D. C., doi:10.2204/iodp.proc.311.213.2010

Riedel, M., M. M. Côté, P. J. Neelands, K. Obana, R. Wania, A. Price, and S. Taylor (2014), Report of Cruise 2010007PGC, C.C.G. Vessel John P. Tully, 30 June – 10 July 2010, SeaJade-I Seafloor Earthquake Array - Japan Canada Cascadia Experiment, Ocean bottom seismometer recovery, methane gas-plume acoustic imaging, and CTD-water sampling program, *Geological Survey of Canada*, 85 pp, doi:10.4095/295545.

Römer, M., H. Sahling, T. Pape, A. Bahr, T. Feseker, P. Wintersteller, and G. Bohrmann (2012a), Geological control and magnitude of methane ebullition from a high-flux seep area in the Black Sea: The Kerch seep area, *Mar. Geol.*, *319–322*, 57–74.

Römer, M., H. Sahling, T. Pape, V. Spiess, and G. Bohrmann (2012b), Quantification of gas bubble emission from submarine hydrocarbon seeps at the Makran continental margin (offshore Pakistan), *J. Geophys. Res.*, *117*, C10015, doi:10.1029/2011JC007424.

Sahling, H., et al. (2009), Vodyanitskii mud volcano, Sorokin trough, Black Sea: Geological characterization and quantification of gas bubble streams, *Mar. Pet. Geol.*, *26*(9), 1799–1811.

Satake K., K. Shimazaki, Y. Tsuji, and K. Ueda (1996), Time and size of a giant earthquake in Cascadia inferred from Japanese tsunami records of January 1700, *Nature*, *379*, 246–249.

Sauter, E. J., S. I. Muyakshin, J.-L. Charlou, M. Schlüter, A. Boetius, K. Jerosch, E. Damm, J.-P. Foucher, and M. Klages (2006), Methane discharge from a deep-sea submarine mud volcano into the upper water column by gas hydrate-coated methane bubbles, *Earth Planet. Sci. Lett.*, *243*, 354–365.

Scandella, B. P., C. Varadharajan, H. F. Hemond, C. Ruppel, and R. Juanes (2011), A conduit dilation model of methane venting from lake sediments, *Geophys. Res. Lett.*, *38*, L06408, doi:10.1029/2011GL046768.

Scandella, B. P., L. Pillsbury, T. Weber, C. Ruppel, H. F. Hemond, and R. Juanes (2016), Ephemerality of discrete methane vents in lake sediments, *Geophys. Res. Lett.*, *43*, 4374–4381, doi:10.1002/2016GL068668.

Shakova, N., I. Semiletov, A. Salyuk, V. Yusupov, D. Kosmach, and Ö. Gustafsson (2010), Extensive methane venting to the atmosphere from sediments of the east Siberian Arctic shelf, *Science*, *327*, 1246–1250.

Spence, G. D., N. R. Chapman, R. D. Hyndman, and C. Cleary (2001), Fishing trawler nets massive "Catch" of methane hydrates, *EOS*, *82*(50), 621–627, doi:10.1029/01EO00358.

Suess, E. (2010), Marine cold seeps, in *Handbook of Hydrocarbon and Lipid Microbiology*, edited by K. N. Timmis, pp. 187–203, Springer, Berlin.

Thompson, R. E. (1981), Oceanography of the British Columbia Coast, *Can. Spec. Publ. Fish. Aquat. Sci.*, *56*, 291 pp.

Thomsen, L., C. Barnes, M. Best, R. Chapman, B. Pirenne, R. Thomson, and J. Vogt (2012), Ocean circulation promotes methane release from gas hydrate outcrops at the NEPTUNE Canada Barkley Canyon node, *Geophys. Res. Lett.*, *39*, L16605, doi:10.1029/2012GL052462.

Torres, M. E., J. McManus, D. Hammond, M. A. d. Angelis, K. U. Heeschen, S. L. Colbert, M. D. Tryon, K. M. Brown, and E. Suess (2002), Fluid and chemical fluxes in and out of sediments hosting methane hydrate deposits on Hydrate Ridge, OR, I: Hydrological provinces, *Earth Planet. Sci. Lett.*, *201*, 525–540.

Tryon, M. D., K. M. Brown, M. E. Torres, A. M. Trehu, J. McManus, and R. W. Collier (1999), Measurements of transience and downward fluid flow near episodic methane gas vents, Hydrate Ridge, Cascadia, *Geology*, *27*(12), 1075–1078.

Varadharajan, C., and H. F. Hemond (2012), Time-series analysis of high-resolution ebullition fluxes from a stratified, freshwater lake C8 - G02004, *J. Geophys. Res.*, *117*, G02004, doi:10.1029/2011JG001866.

Walter, K. M., S. A. Zimov, J. P. Chanton, D. Verbyla, and F. S. Chapin (2006), Methane bubbling from Siberian thaw lakes as a positive feedback to climate warming, *Nature*, *443*(7107), 71–75.

Wang, K., and E. E. Davis (1996), Theory for the propagation of tidally induced pore pressure variations in layered subseafloor formations, *J. Geophys. Res.*, *101*(B5), 11,483–11,495, doi:10.1029/96JB00641.

Wang, K., E. E. Davis, and G. van der Kamp (1998), Theory for the effects of free gas in subsea formations on tidal pore pressure variations and seafloor displacements, *J. Geophys. Res.*, *103*(B6), 12,339–12,353, doi:10.1029/98JB00952.

Westbrook, G.K. et al. (Eds.) (1994), Proceedings of the Ocean Drilling Program, *Initial Rep.*, vol. 146 (part 1), Ocean Drill. Program, College Station, Tex.

Whiticar, M. J., R. Wania, A. Price, G. Spence, and M. Riedel (2010), Character and Fate of Methane Plumes from Sediments on the North Cascadia Margin, Abstract OS52B-01 presented at 2010 Fall Meeting, AGU, San Francisco, Calif., 13–17 Dec.

Willoughby, R. Mir, C. Scholl, and R. N. Edwards (2008), Neptune-Canada based geophysical imaging of gas hydrate in the Bullseye Vent, in *Proceedings of the 6th International Conference on Gas Hydrates (ICGH 2008), University of British Columbia, Vancouver, Canada*, 6–10 July.

Yuan, T., R. D. Hyndman, G. D. Spence, and B. Desmons (1996), Seismic velocity increase and deep-sea gas hydrate concentration above a bottom-simulating reflector on the northern Cascadia continental slope, *J. Geophys. Res.*, *101*(B6), 13,655–13,671, doi:10.1029/96JB00102.

Zyla, T. (2011), Tracking methane bubble plumes on the northern Cascadia margin, BSc. Thesis, Univ. of Victoria, Victoria, British Columbia, Canada.